ELSEVIER

Contents lists available at ScienceDirect

Materials Science & Engineering A

journal homepage: www.elsevier.com/locate/msea





Computationally guided alloy design and microstructure-property relationships for non-equiatomic Ti–Zr–Nb–Ta–V–Cr alloys with tensile ductility made by laser powder bed fusion

Dillon Jobes ^{a,1}, Daniel Rubio-Ejchel ^{a,1}, Lucero Lopez ^c, William Jenkins ^b, Aditya Sundar ^c, Christopher Tandoc ^d, Jacob Hochhalter ^b, Amit Misra ^c, Liang Qi ^c, Yong-Jie Hu ^d, Jerard V. Gordon ^{a,c,*}

- ^a Department of Mechanical Engineering, University of Michigan, Ann Arbor MI, 48109, USA
- b Department of Mechanical Engineering, University of Utah, Salt Lake City, UT 84112, USA
- ^c Department of Materials Science and Engineering, University of Michigan, Ann Arbor, MI, 48109, USA
- ^d Department of Materials Science and Engineering, Drexel University, Philadelphia, PA 19104, USA

ARTICLEINFO

Keywords: Additive manufacturing Machine learning Alloy design Rapid solidification Refractory high entropy alloys Microstructure

ABSTRACT

Single-phase body-centered cubic refractory complex concentrated alloys (RCCAs), exhibit strength retention at temperatures above the melting points of conventional Ni-based superalloys. However, their lack of room temperature tensile ductility leads to cracks during processing and/or premature failure under mechanical loading when fabricated by laser-based metals additive manufacturing (AM). We present an alloy design framework for tensile ductility in non-equimolar RCCAs amenable to AM processing within the Ti-V-Cr-Nb-Zr-Ta system. First, density functional theory (DFT) and machine learning informed screening of alloy compositions were used to down-select $\sim 10^6$ alloys with potential for tensile ductility. Next, Scheil solidification modeling was used to eliminate compositions most at risk for micro-segregation and solidification cracking based on the estimated freezing range of each alloy. This led to the design of two new, representative alloys: $Ti_{0.4}Zr_{0.4}Nb_{0.1}Ta_{0.1} \text{ and } Ti_{0.486}V_{0.375}Ta_{0.028}Cr_{0.111}. \text{ These alloys were evaluated for rapid solidification } Ti_{0.486}V_{0.375}Ta_{0.028}Cr_{0.111}.$ defect formation using in-situ synchrotron melt pool imaging, fabricated via laser powder bed fusion (L-PBF) AM, and then characterized for processing defects, microstructure, and mechanical properties. Overall, both alloys achieved tensile yield strengths >800 MPa and failure strains >5 %. However, the occurrence of un-melted powders of high melting point elements likely resulted in premature failure during tensile straining. Considerations about mitigating this defect source are discussed and the role of local micro-segregation on ductility are elucidated. Overall, these results highlight the success of our framework, and show potential for laser-based AM-RCCAs with tensile ductility.

1. Introduction

The design, synthesis, and processing of BCC refractory complex concentrated alloys (RCCAs) has undergone rapid development since the first identified composition (the equiatomic MoNbTaW alloy) reported by Senkov et al., [1]. While FCC multi-component alloys have been also been investigated (e.g. CrCoNi-based high entropy alloys), Ti-based RCCAs, such as Nb $_{45}$ Ta $_{25}$ Ti $_{15}$ Hf $_{15}$ and HfNbTaTiZr, have shown enhanced strength/ductility synergy resulting from the activation of

multiple slip systems during deformation [2]. Single-phase BCC RCCAs containing high concentrations of elements from Group IV (Ti, Zr, Hf), Group V (V, Nb, Ta), and Group VI (Cr, Mo, W) families possess excellent strength and strength retention under extreme environments and show potential as successors to conventional Fe- and Ni-based superalloys in next generation power sources as a result of significant solid solution strengthening maintaining high strength at elevated operation temperatures, increasing turbine efficiency [3]. However, most RCCAs contain large amounts of high-melting temperature elements, which negatively

E-mail address: jerardvg@umich.edu (J.V. Gordon).

 $^{^{\}ast}$ Corresponding author.

¹ Equal Contribution.

impacts their room-temperature ductility and fracture toughness. Overall, this lack of room temperature ductility and fracture toughness is a major concern that significantly hinders both manufacturing and in-service applications of many candidate alloys.

The need to enhance room-temperature ductility and toughness originates from a desire to fabricate near-net-shaped components across multiple sectors [4]. However, conventional synthesis and processing routes for RCCAs are complicated by large differences in melting temperatures of constituent elements which can make it difficult to produce bulk materials with homogeneous structure and composition using standard arc or induction melting techniques [5]. Additionally, subtractive manufacturing methods may be impractical (or impossible) for RCCAs containing a high percentage of refractory metals. Importantly, the microstructures of as-cast alloys are sensitive to the solidification rate; increasing solidification rates have been shown to reduce micro segregation, refine grain size, and result in higher microhardness values compared to conventional cast alloys [6–8]. This highlights the potential for paradigm changing rapid solidification techniques such as metals additive manufacturing (AM) to take advantage of these benefits.

While prevalent in the literature, studies on AM-RCCAs have led to mixed successes; in general, only a subset of potential candidates were successfully printed without significant manufacturing defects such as solidification cracking and keyhole porosity. Only a small number of fully-dense RCCA candidates successfully printed via metal AM have shown tensile ductility (i.e., [9-11]). This is because process outcomes for AM-RCCAs largely depend on both material composition and AM process variable selection; for example, low melting temperature Nb content was depleted in laser powder bed fusion (L-PBF) MoNbTaW [12] due to significant elemental vaporization, as opposed to an increased Nb content in directed energy deposition (DED) MoNbTaW [8] wherein a propensity for complete melting has more influence on final composition. Furthermore, large macroscopic porosity and cracks were discovered for DED MoNbTaW [8] as compared to fully dense L-PBF MoNbTaW in Ref. [12] due to non-optimal processing parameter selections. Depending on the freezing range of specific alloy compositions, solidification cracking defects may occur even for relatively ductile compositions. These studies point to the difficulty in rapid solidification processing of RCCAs, and the need for a robust alloy design framework considering AM processing science.

In this study, we leverage an alloy design strategy for L-PBF of representative RCCAs from the Ti-V-Cr-Nb-Zr-Ta system with room temperature ductility based framework spanning multiple length scales: (i) alloy screening by first-principles density functional theory (DFT) aided machine learning, (ii) Scheil solidification modeling for hot cracking susceptibility, (iii) melt pool level in situ synchrotron dynamic x-ray radiography (DXR) imaging to develop a process map avoiding laser-material interaction defects, and (iv) laser powder bed fusion (L-PBF) AM printing of bulk samples for mechanical testing. We employ a DFT-based machine learning model on the atomistic scale to predict alloys with ductility potency based on our prior work [13] [15], then leverage thermodynamic calculations using the CALculation of the PHAse Diagram (CALPHAD) approach for the assessment of phase stability and AM printability. This framework was applied to manufacture two, non-equiatomic alloys using L-PBF AM: (i) Ti_{0.4}Zr_{0.4}Nb_{0.1}Ta_{0.1} and (ii) $Ti_{0.486}V_{0.375}Ta_{0.028}Cr_{0.111}$, which were tested under uniaxial tension loading. While other studies have largely focused on trial-and-error type approaches to identify alloy compositions for AM-RCCAs (i.e., based on previously known ductile compositions) [10], our framework is specifically designed to be robust and predictive, leveraging physics-based models of arbitrary combinations of elements to determine potential compositions. As such, the framework can be extended to consider alloys with potential applications for both room temperature and high-temperature performance.

2. Materials and methods

2.1. First-principles calculations and ML-based surrogate modeling

First-principles calculations based on density functional theory (DFT) were combined with a ML regression approach to develop surrogate models that can efficiently predict the unstable stacking fault energy, γ_{usf} and surface energy γ_{surf} for the $\langle 111 \rangle \{110\}$ slip system in multicomponent BCC alloys according to their chemical compositions (Fig. 1a), following computational approaches developed earlier [13–17]. Specifically, DFT calculations were performed to sample γ_{usf} and γ_{surf} for a series of binary, ternary, and multicomponent compositions. The calculation results were separated into training and validation datasets to develop the surrogate models using a ML-based regression method established in our prior research. The regression was carried out with a set of physics-based descriptors from a bond-counting model and atomistic/electronic structure feature parameters. More detailed elucidation on the model construction can be found in Ref. [13] A systematic prediction of γ_{usf} and γ_{surf} was performed using the developed surrogate models across various alloy compositions to search for candidates that may have enhanced strength-ductility synergies in a vast compositional space containing Groups IV-VIII elements (i.e., Ti, Zr, V, Nb, Ta, Mo, W, Re, and Ru) and oxide forming elements (i.e., Al, Cr). Note: due to the high pyrophoricity of Hf powders (for follow on AM printing using elemental powder blends), Hf was omitted from the overall screening. For every alloy composition, its D parameter was calculated as D = $\gamma_{\text{surf}}/\gamma_{\text{usf}}$ to evaluate whether the alloy is intrinsically ductile according to the Rice model [13,18]. The Rice model attributes the intrinsic brittleness and ductility of a bulk material to a competition between continuous crack propagation and dislocation emission at a crack tip. The ease of crack propagation can be related to γ_{surf} of the cleavage crystal plane, while ease of dislocation emission can be related to γ_{usf} based on the Peierls-Nabarro model of dislocation formation and movement. Therefore, a higher ratio of $\gamma_{surf}/\gamma_{usf}$, i.e. a larger D, would imply plastic deformation associated with dislocation emission is more likely to happen at a crack tip rather than a brittle cleavage fracture, consequently leading to better ductility.

Additionally, our previous work indeed uncovered that values of the D parameter show strong positive correlations with the experimentally measured compression fracture strain of many RCCAs [13]. Particularly, the RCCAs with a compression fracture strain larger 40 % were found to have D > 3.0 in general [19]. Since high fracture strain under compression is a necessary (but not sufficient) condition for to achieve high ductility, these correlations indicate that this D parameter is effective for the first-step screening of RCCAs ductility. Among the initially screened $\sim 10^6$ alloys, approximately $\sim 10^4$ alloys had D > 3.0, which were further screened for AM printability via Scheil solidification simulation using the Thermo-Calc Software and the TCHEA4 database [20] and the Kou hot cracking model [21,22] compared to values for 316L stainless steel and H13 tool steel which are L-PBF AM printable materials. Fig. 1b demonstrates the hot crack susceptibility index, wherein a higher value of $|dT/d\sqrt{f_s}|$, in which *T* is temperature and f_s is the solid fraction in the semisolid, near $\sqrt{f_s} = 1.0$ indicates a propensity for cracking defects. These selection steps led to approximately $\sim 10^2$ alloys, from which two representative alloys were chosen overall: Ti_{0.4}Zr_{0.4}Nb_{0.1}Ta_{0.1} and Ti_{0.486}V_{0.375}Ta_{0.028}Cr_{0.111} (values in at. fraction). These two alloys were considered as "representative" as they considered a range of D parameter values, freezing ranges, and solidification gradients (Table 1) which influence material performance and susceptibility to cracking during solidification [22]. In particular, these alloys were specifically selected to have a small freezing range (<100 °C) as this typically reduces the susceptibility to solidification crack formation and micro segregation under AM processing [21,23]. The CALPHAD predicted phase diagrams in Fig. 1 c and d show single-phase BCC structure above 1200 °C for both alloys.

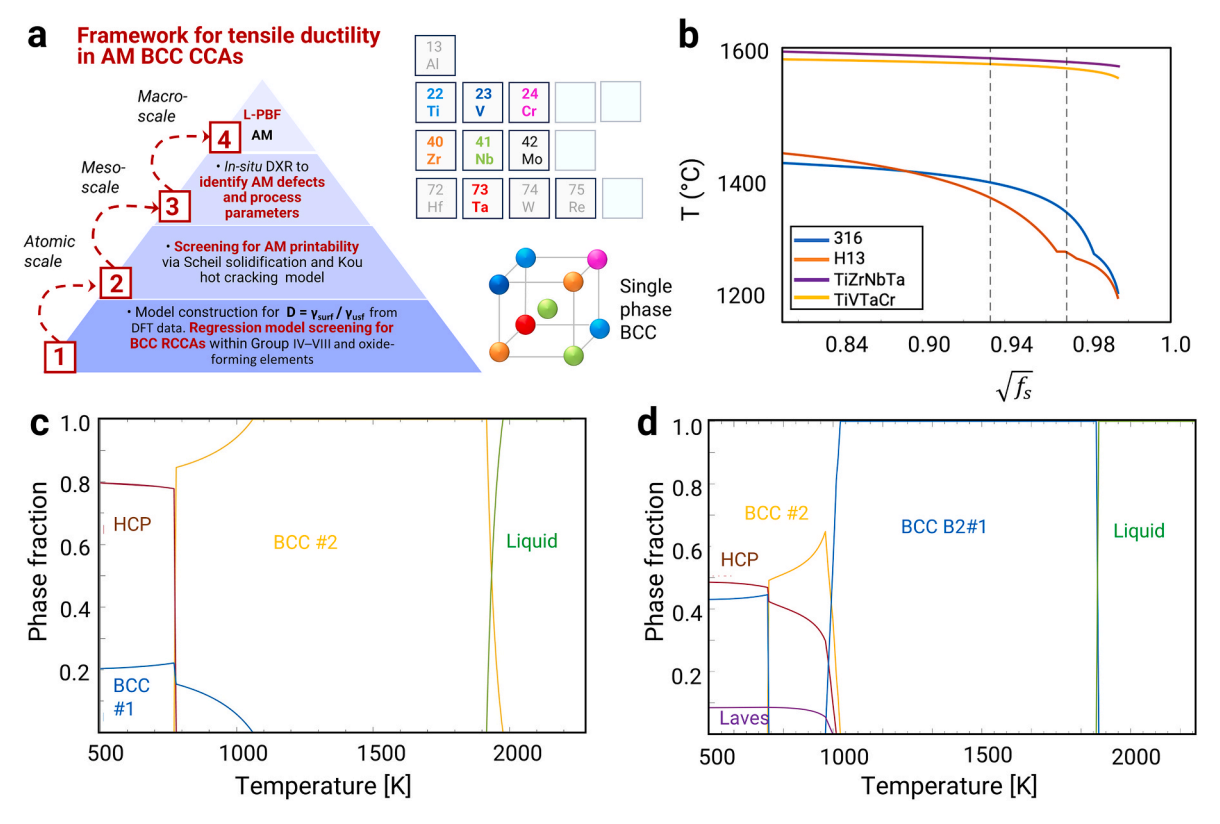


Fig. 1. Framework for tensile ductility in RCCAs made by L-PBF AM using (a) first-principles and surrogate ML model screening of ductile compositions with D > 3.0. (b) Alloys were additionally screened for L-PBF printability via Scheil solidification and Kou hot cracking model. Predicted CALPHAD phase diagram of down-selected alloys: (c) $Ti_{0.4}Zr_{0.4}Nb_{0.1}Ta_{0.1}$ and (d) $Ti_{0.486}V_{0.375}Ta_{0.028}Cr_{0.111}$.

Table 1Atomistic and thermophysical material parameters for both selected compositions.

	-		-			
Composition	$\gamma_{\text{surf}} (J/m^2)$	$\gamma_{\rm usf} ({\rm J/m}^2)$	D-parameter	T_{melt} (°C)	Freezing Range (°C)	$dT/df_s^{1/2}$ (°C)
Ti _{0.4} Zr _{0.4} Nb _{0.1} Ta _{0.1}	1.67	0.44	3.8	1642	60.3	193.3
$Ti_{0.486}V_{0.375}Ta_{0.028}Cr_{0.111}$	2.01	0.64	3.1	1598	10.2	93.3

2.2. In-situ DXR experiments and process modeling for keyhole and LOF defects

To quantify the potential occurrence of laser-powder interaction defects during rapid solidification (e.g., solidification crack formation and porosity transfer) and to develop a processing map for follow on L-PBF AM printing, in-situ DXR experiments were conducted at the 32-ID-B beamline of the Advanced Photon Source at Argonne National Laboratory [24-26]. DXR provides real-time imaging of defect transfer and can be employed as a high-throughput analysis technique; Importantly, this is not possible using standard single-bead experiments and destructive analysis. Model material discs of Ti_{0.4}Zr_{0.4}Nb_{0.1}Ta_{0.1} and Ti_{0.486}V_{0.375}-Ta_{0.028}Cr_{0.111} were fabricated using vacuum arc melting (Sophisticated Alloys Inc) and homogenized at 1200 °C for 24 h in an inert atmosphere (Fig. 1c and d) [25,26]. After furnace cooling, rectangular 40 mm long, 3 mm tall and 0.4 mm thick specimens were extracted using wire EDM for in-situ DXR experiments. In more detail, high-energy x-rays were used to directly visualize laser-matter interaction defects including solidification cracking and porosity formation under conditions representative of L-PBF for both RCCAs samples. This was done by simultaneously illuminating an area containing the melt pool and vapor cavity using polychromatic x-rays while a scanning laser impinged across the long edge of the specimen. Incoming x-rays transmitting through the sample thickness were collected on a scintillator and transformed to visible light images that were captured using a

high-speed camera placed behind at a frame rate of 50 kHz and spatial resolution of 2 $\mu m.$ An ytterbium fiber scanning laser with wavelength of 1070 nm, spot size of 80 μm , and a Gaussian beam profile was used to provide laser power (P) between 150 W < P < 450 W. A galvo scanner enabled the laser to scan across the sample surface at speeds between 0.3 < V < 1.2 m/s. Approximately 30 experiments were recorded for each RCCA specimen to evaluate the influence of different combinations of P–V on defect formation. All experiments were performed under 1 atm Ar protective gas and with no powder layer on top. Postprocessing of the DXR images was undertaken using a custom python script to enhance features of interest using background division [12].

Optimized L-PBF printing parameters were selected using a combination of *in-situ* DXR results and Rosenthal-based melt pool geometry estimation to identify the process window for both compositions. In more detail, the Rosenthal equation (1) is a well-established solution to the differential equation modeling the steady state temperature field of a moving point source of heat on an infinite plane.

$$T = T_0 + \frac{Q}{2\pi kR} \exp\left(\frac{V(z-R)}{2\alpha}\right) \tag{1}$$

Where T is the temperature at the location of interest, T_0 is the temperature at infinity, Q is the absorbed power, V is the velocity of the moving point source, k is the thermal conductivity, α is the thermal diffusivity, and R is the distance of the point of interest to the point source $(R = \sqrt{x^2 + y^2 + z^2})$. Using this equation, plugging in the

melting temperature T_m of the material for T and rearranging, the depth (D) of the melt pool boundary can be approximated. The manipulated equation (2) can be seen below.

$$D = \sqrt{\frac{2Q}{\pi \rho e C_p V(T_m - T_0)}} \tag{2}$$

Where ρ is the material density and C_p is the heat capacity. Using this, and assuming a hemispherical melt pool (the width (W) is twice the depth). These predicted dimensions of the melt pools were then used to find appropriate processing parameters using the geometric lack of fusion equation (3) [27].

$$\left(\frac{H}{W}\right)^2 + \left(\frac{L}{D}\right)^2 \le 1\tag{3}$$

Where H is hatch spacing and L is layer height. Having a value that is less than one indicates geometrically that the sample should be fully dense, and above one the sample should show the lack of fusion defect caused by incomplete melting.

To calculate the keyhole melt pool boundary, normalized enthalpy was calculated based on ratio between deposited energy density (ΔH) to the enthalpy at melting (h_s), or:

$$\frac{\Delta H}{h_{sm}} = \frac{AP}{\pi h_{s} \sqrt{\alpha v a^{3}}} > \frac{\pi T_{b}}{T_{m}} \tag{4}$$

Where T_b is the boiling temperature, T_m is the melting temperature, where A is the laser absorptance, P is the laser power, α is the thermal diffusivity, ν is the scan speed, and a is the beam radius. Normalized enthalpy has been recently demonstrated to be effective in quantifying the relationship between the laser absorption and cavity depth under transient conditions using DXR imaging of Ti–6Al–4V [28]; thus, it's use in this study is justified. Importantly, keyhole melt pools do not guarantee keyhole pores, but unstable keyholes create the opportunity for keyhole porosity. Keyhole melt pools were quantified as possessing a depth to width ration (D/W) greater than 0.5. Table 2 provides the thermophysical quantities used in process modeling for each alloy. These thermophysical quantities were calculated using the CALPHAD approach and the TCHEA4 database.

2.3. Bulk L-PBF processing

Elemental powder blends of and Ti, Zr, Nb, and Ta $(Ti_{0.4}Zr_{0.4}Nb_{0.1}Ta_{0.1})$ and Ti, V, Cr, and Ta $(Ti_{0.486}V_{0.375}Ta_{0.028}Cr_{0.111})$ were separately mixed in batches for approximately 1 h in an Inversina 2L tumbler-mixer to create powder blends (Fig. 2a). Elemental powders were used instead of pre-alloyed powders for L-PBF AM in this study based on a few important considerations, namely their recent (and common usage) to manufacture defect-free bulk AM-RCCA samples in other studies in the literature such as [29,30], their enhanced cost-effectiveness, and the difficulty in sourcing customized, pre-alloyed powders from industrial sources. Additionally, the use of elemental enables high-throughput assessment process-structure-property relationships for arbitrary compositions; something that is not feasible via pre-alloyed powders. Powder sizes ranged in size between 15 and 45 µm, and (except for Zr powders) possessed spherical geometries. The use of non-spherical elemental Zr was chosen since spherical Zr powders possess extremely high

pyrophoricity.

Elemental powder blends were printed on the L-PBF AM (DiAM) system at Lawrence Livermore National Lab (LLNL) within an Ar protective gas environment [31]. Unlike in Ref. [31], this work did not employ the secondary diode laser for preheating or *in-situ* annealing. Process mapping experiments were used to determine the optimal parameter selection for each alloy based on Archimedes density using cubes of approximately 10 mm³. Optimized process variables were determined as follows for both compositions: laser power of 250 W, scan speed of 750 mm/s, hatch spacing of 90 μ m, Layer thickness of 40 μ m. Bulk rectangular geometries of approximately 22 mm long, 8 mm tall, and 5 mm wide (Fig. 2b) were fashioned using optimized parameter sets for follow on mechanical testing and microstructural characterization.

2.4. Tensile testing

Displacement-controlled tensile testing was completed to measure the tensile strength and ductility of the AM-RCCAs. Two tests were completed for the two compositions using sub-size specimens with gage width of 1.20 mm (Fig. 2c). All the samples were made and tested from the orientation orthogonal to the build direction. Testing was performed using a servo-electric test stand at a displacement rate of 0.1 mm/min, per the ASTM E8 standard, until failure. Force was recorded during the test using a 1 kN load cell and engineering stress was computed by dividing by the initial cross-sectional area. Strain was measured from digital image correlation (DIC) using VIC 2D software. One DIC image per second was using a five MP camera. The coupons were prepped for DIC by spray painting the gauge section white and adding a black speckle pattern using an airbrush. The speckle size was small enough to capture the small changes in strain across the length of the coupon; each speckle measured about 6-10 pixels in diameter. A subset size of 39 pixels was used to ensure each subset contained 3x3 speckles. With this subset size, a noise floor of 250 microstrain was achieved. The strain data that was exported from VIC 2D was quantified using a virtual extensometer spanning the length of the gauge section of the coupon.

2.5. Microstructural characterization

Microstructure was characterized using scanning electron microscopy (SEM), electron backscatter diffraction (EBSD), and energy dispersive spectroscopy (EDS) after each sample surface was ground and polished to EBSD quality using colloidal SiO₂. SEM, EBSD, and EDS data were taken on a TESCAN MIRA-3 FEG (beam energy of 30 keV) at the University of Michigan Center for Materials Characterization. X-ray diffraction (XRD) was performed to quantify bulk phase information using a Rigaku Smart Lab XRD at 40 keV.

3. Results

3.1. In situ DXR and process modeling results

Fig. 3 compares the *in-situ* DXR experiments with process modeling for LOF and keyhole defect boundaries. It is readily evident that the melt pool morphologies for both samples follow systematic trends within P–V process space; low laser powers and high scanning velocities result in shallow melt pools, whereas high powers and low velocities lead to significant increases in depth-to-width aspect ratio (D/W) indicating keyhole melt pools. Intermediate selections of power and velocity show

Table 2Thermophysical parameters used in process modeling.

Composition	Density (g/cm ³)	Heat capacity (J/K/mol)	Boiling Point (K)	Specific Enthalpy (kJ/mol)	Diffusivity (m ² /s)	Laser Absorptance
$\begin{array}{c} {\rm Ti_{0.4}Zr_{0.4}Nb_{0.1}Ta_{0.1}} \\ {\rm Ti_{0.486}V_{0.375}Ta_{0.028}Cr_{0.111}} \end{array}$	6.93	25.48	3903	7.742	1.37E-05	0.24
	5.65	25.08	3239	6.141	1.11E-05	0.21

Fig. 2. (A) Elemental powder blends were used to manufacture both compositions using (b) L-PBF on the DiAM system at LLNL. (c) Sub-sized samples were removed from bulk materials and tested under uniaxial tension to failure.

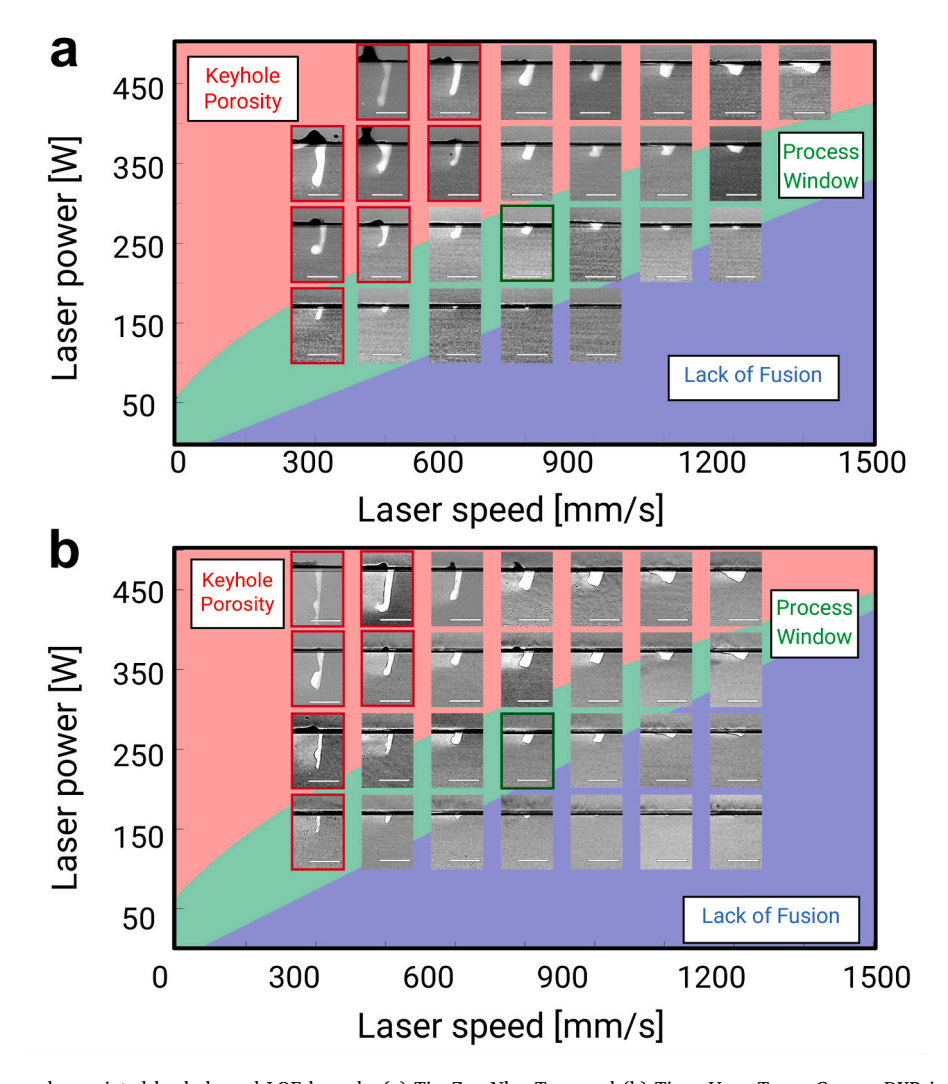


Fig. 3. In-situ DXR images and associated keyhole and LOF bounds: (a) $Ti_{0.4}Zr_{0.4}Nb_{0.1}Ta_{0.1}$ and (b) $Ti_{0.486}V_{0.375}Ta_{0.028}Cr_{0.111}$. DXR images with red outlines in keyhole regime possess D/W > 0.5 and showed the formation of keyhole porosity. (For interpretation of the references to color in this figure legend, the reader is referred to the Web version of this article.)

semicircular melt pool, indicative of conduction mode melting. DXR results also showed limited keyhole porosity development where only melt pools with D/W greater than D/W = 0.5 showed keyhole porosity in the high-P/low-V regions [26]. Interestingly, all keyhole melt pools for both compositions evaluated in this study were discovered to generate keyhole porosity. These melt pools are outlined in red boxes in Fig. 3. In comparison, only a small subset of process variables showed incomplete melting indicating LOF defects. Comparatively, process modeling provides the lower bound of the process window (equation (3)) in blue denoting LOF porosity whereas the upper boundary of the process window (equation (4)) denoting keyhole melt pools is shown in red in Fig. 3a and b. Overall, process modeling for the LOF and keyhole

defect boundaries show good agreement with DXR images and enabled the selection of optimized process variables within the process window (green regions of Fig. 3) of each alloy for follow on AM processing. Overall, solidification crack formation was not discovered during *in situ* DXR measurements across all P–V combinations for either alloy. This highlights the success of our screening approach for L-PBF printability.

3.2. Tensile testing

Tensile results for both alloys are presented in Fig. 4. An example of room temperature testing behavior for Ti_{0.4}Zr_{0.4}Nb_{0.1}Ta_{0.1} is presented in Fig. 4a. It is evident that the composition possesses tensile ductility

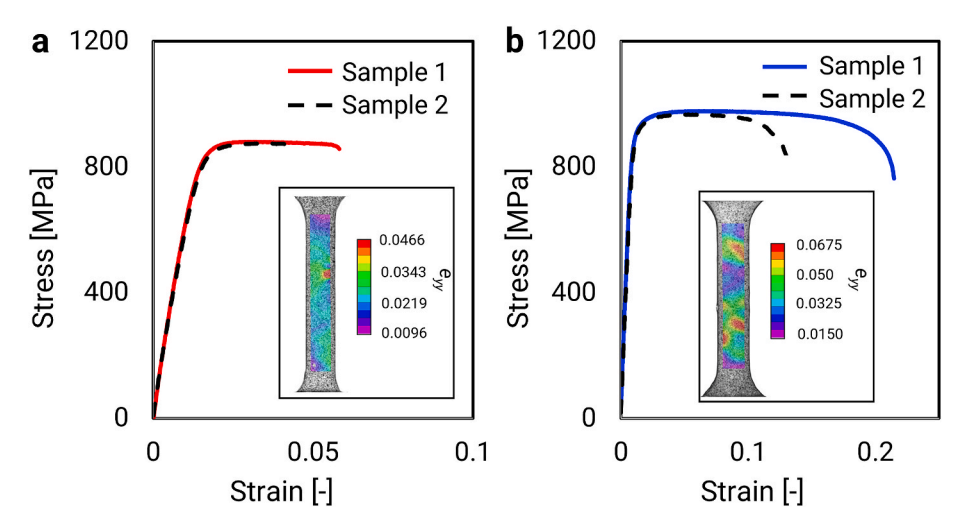


Fig. 4. Engineering stress-strain for curves for: (a) $Ti_{0.4}Zr_{0.4}Nb_{0.1}Ta_{0.1}$ and (b) $Ti_{0.486}V_{0.375}Ta_{0.028}Cr_{0.111}$. Insert showing single DIC image of full-field strain development during tensile testing.

(defined as >4 % uniform strain to failure in Ref. [9]), reaching a strain to failure of 5.1 ± 0.7 % (Table 3). Overall, the tensile properties are similar to other β -Ti alloys made by L-PBF, with Young's Modulus of $E=59\pm0.2$ GPa and yield strength of $\sigma_y=819\pm1.4$ MPa in the as-built AM state. Additionally, little to no strain hardening is evident up to sample fracture. Comparatively, the tensile results for $Ti_{0.486}V_{0.375}$ - $Ta_{0.028}Cr_{0.111}$ are presented in Fig. 4b. This alloy possesses enhanced yield strength ($\sigma_y=879\pm2.2$ MPa) and increased ductility (failure strain of $\epsilon_f=17.7\pm3.7$ %) compared to $Ti_{0.4}Zr_{0.4}Nb_{0.1}Ta_{0.1}$.

This difference in tensile behaviors between $Ti_{0.4}Zr_{0.4}Nb_{0.1}Ta_{0.1}$ and $Ti_{0.486}V_{0.375}Ta_{0.028}Cr_{0.111}$ can be understood based on higher unstable stacking fault energy $\gamma_{usf,B} = 0.64~J/m^2$ versus $\gamma_{usf,A} = 0.44~J/m^2$. Since γ_{usf} is related to yield strength, higher values of σ_y in composition can be expected. Additionally, $Ti_{0.486}V_{0.375}Ta_{0.028}Cr_{0.111}$ has a higher modulus of 100 GPa, closer to HCP α -Ti. This can be partially explained due to the high percentage of titanium [32,33], but is nevertheless interesting given the large concentration of V and Cr (both β stabilizers). Overall, both alloys exhibited yield strengths >795 MPa and strains to failure >6% highlighting the power of our screening framework for identifying alloys with ductility potency.

3.3. As-built microstructure and phase distribution

The as-built microstructure for both compositions is presented in Fig. 5. $Ti_{0.4}Zr_{0.4}Nb_{0.1}Ta_{0.1}$ and $Ti_{0.486}V_{0.375}Ta_{0.028}Cr_{0.111}$ show microstructures and complex grain morphologies typically observed for metals undergoing rapid solidification processing. $Ti_{0.4}Zr_{0.4}Nb_{0.1}Ta_{0.1}$ possesses a smaller average grain size of $33.2~\mu m$, versus $42.3~\mu m$ for $Ti_{0.486}V_{0.375}Ta_{0.028}Cr_{0.111}$ (Table 3). However, both samples suffer from incomplete melting of powder particles likely attributed to non-optimal processing variables (Fig. 5b and f). This is shown by energy dispersive spectroscopy (EDS) results which indicates that these particles are largely Nb and Ta in $Ti_{0.4}Zr_{0.4}Nb_{0.1}Ta_{0.1}$, and un-melted powders in $Ti_{0.486}V_{0.375}Ta_{0.028}Cr_{0.111}$ largely consist of V and Cr elements (Fig. 5c and 9)

X-ray diffraction (XRD) of both alloys confirm that the bulk phase distribution of $Ti_{0.4}Zr_{0.4}Nb_{0.1}Ta_{0.1}$ and $Ti_{0.486}V_{0.375}Ta_{0.028}Cr_{0.111}$

exhibit the prominent single-BCC phase expected for these alloys (Fig. 1c and d); this is consistent with previously published literature for TiNbZrTa and TiVCrTa [34-38] (Fig. 6). Interestingly, the incomplete melting of powder particles is evident by extraneous peaks for constituent elements in Fig. 6 (i.e., Ta, Nb, and Ti in Ti_{0.4}Zr_{0.4}Nb_{0.1}Ta_{0.1} and Ta in $Ti_{0.486}V_{0.375}Ta_{0.028}Cr_{0.111}$). However, due to the distribution of the un-melted particles and their size relative to the measurement volume, the occurrence and significance of these elements in a particular scan is variable based on what is locally captured in the specific scan volume. For example, while the presence of un-melted elemental V can be observed in Ti_{0.486}V_{0.375}Ta_{0.028}Cr_{0.111} (Fig. 5g), these particles were not captured in the XRD sample volume and elemental V peaks are absent. Additionally, the relatively high peak intensity of some elemental planes may be attributed to a disproportionately high concentration of corresponding particles in the scan volume. Furthermore, many of these constituent elements also share similar peak positions to one another resulting in additive peak intensities as well as broadening at some of these positions. These results for microstructure and phase distribution show that un-melted powder particles likely influence both mechanical behavior and chemical heterogeneity of the samples and as such will be further discussed in Section 4.1, where the samples with less deleterious defects (e.g., Sample 1 for each composition), will be evaluated.

4. Discussion

4.1. Role of composition, microstructure, and defects on tensile performance

Single-phase BCC RCCAs containing high concentrations of elements from Group IV (Ti, Zr, Hf), Group V (V, Nb, Ta), and Group VI (Cr, Mo, W) families possess excellent strength and strength retention under extreme environments. However, significant differences in both strength and ductility between compositions were observed. While differences in yield strength were anticipated based on unstable stacking fault energy, the significant variation in tensile strain to failure for $Ti_{0.4}Zr_{0.4}Nb_{0.1}Ta_{0.1}$ ($\epsilon_{failure}=6$ %) versus $Ti_{0.486}V_{0.375}Ta_{0.028}Cr_{0.111}$ ($\epsilon_{failure}=21.5$ %) necessitates further consideration.

Table 3 Mechanical and microstructure properties.

Composition	EDS Composition (at. fraction)	E (GPa)	σ _y (MPa)	σ _{UTS} (MPa)	$\varepsilon_{\mathrm{failure}}$ (%)	Avg grain size (μm)
Ti _{0.4} Zr _{0.4} Nb _{0.1} Ta _{0.1}	${ m Ti_{0.31}Zr_{0.28}Nb_{0.28}Ta_{0.14}} \ { m Ti_{0.49}V_{0.36}Cr_{0.12}Ta_{0.03}}$	59 ± 0.2	819 ± 1.4	877 ± 2.9	5.1 ± 0.7	33.2
Ti _{0.486} V _{0.375} Ta _{0.028} Cr _{0.111}		95 ± 3.5	879 ± 2.2	972 ± 5.4	17.7 ± 3.7	42.3

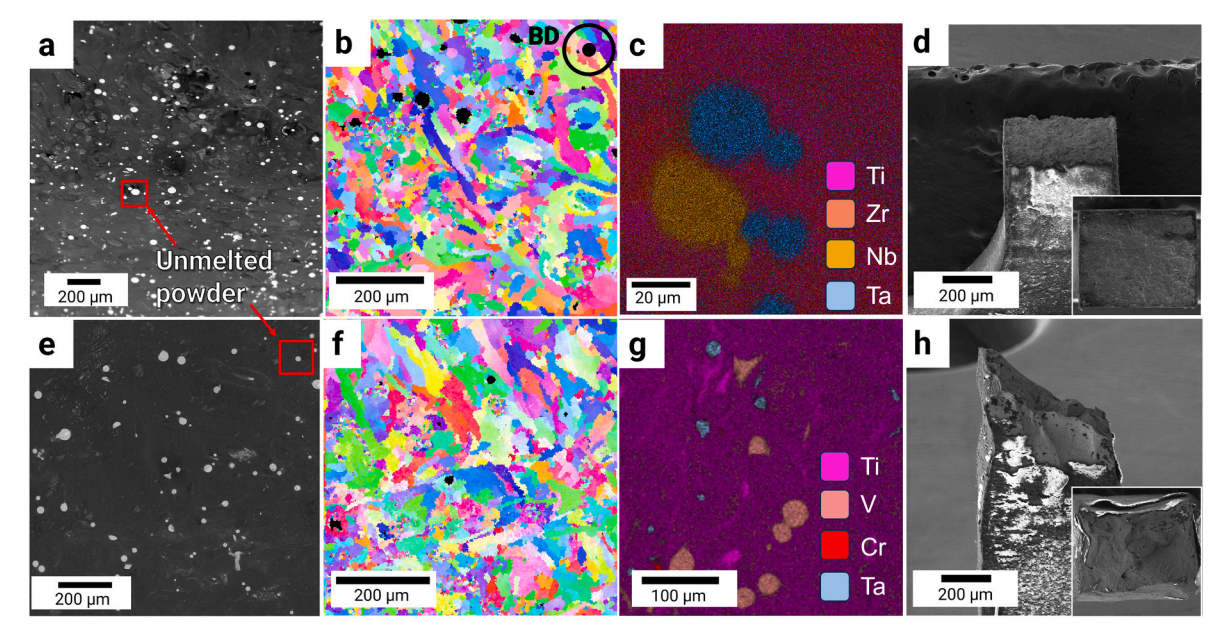


Fig. 5. SEM, EBSD, EDS, and fracture surface images, respectively for: $Ti_{0.4}Zr_{0.4}Nb_{0.1}Ta_{0.1}$ (a–d), and $Ti_{0.486}V_{0.375}Ta_{0.028}Cr_{0.111}$ (e–h). Note: All SEM, EBSD, and EDS images are in taken with the AM build direction oriented into the page.

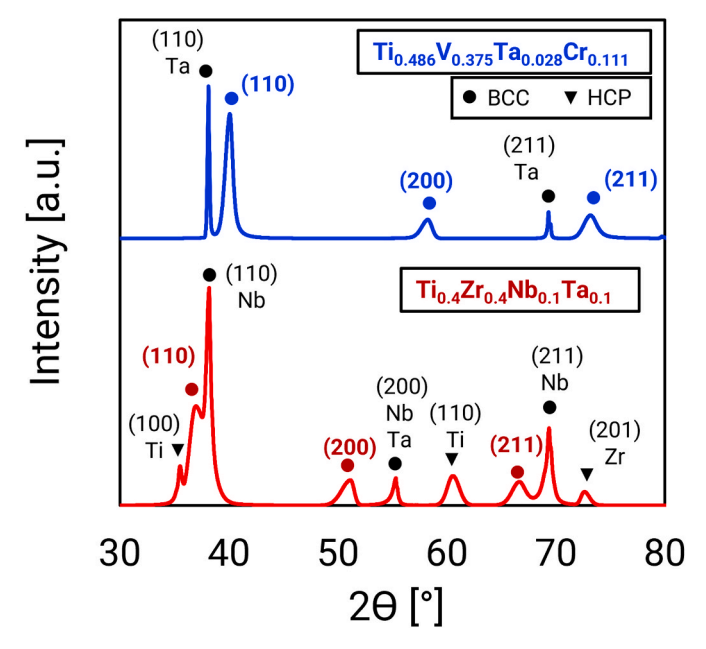


Fig. 6. XRD spectra for $Ti_{0.4}Zr_{0.4}Nb_{0.1}Ta_{0.1}$ and $Ti_{0.486}V_{0.375}Ta_{0.028}Cr_{0.111}$ in asbuilt AM condition. Note nominal single-phase BCC structure of both alloys (denoted in color), with the addition of other BCC (Nb, Ta) and HCP (α -Ti, Zr) phases present from un-melted powder particles denoted in black. (For interpretation of the references to color in this figure legend, the reader is referred to the Web version of this article.)

Since $Ti_{0.4}Zr_{0.4}Nb_{0.1}Ta_{0.1}$ possesses a higher D parameter (D=3.8) compared to $Ti_{0.486}V_{0.375}Ta_{0.028}Cr_{0.111}$ (D=3.1), it is likely that differences in ductility between the compositions can be satisfactorily explained by considering microstructure or AM process-related defects (i.e., porosity and un-melted particles). This is based on our hypothesis that alloys with D>3.0 show ductility tendency. As shown in our prior work [13,14], alloys with D>3.0 show a strong tendence to be intrinsically ductile; however, it is important to note here that this does not indicate that higher values of D certainly correlate with increased ductility. For example, F igure 10 in Ref. [39] shows several alloy cases

with D > 3.0 but low fracture strain measured in experiments, possibly due to the effects of microstructures and/or impurities that cannot predicted by the D parameter. Additionally, the TiZrHfNb and Ti_{1.5}ZrHf_{0.5}Nb_{0.5}Ta_{0.5} alloys have comparable D parameters (\sim 3.8) but show different tensile failure strains (14.9 % vs. 18.8 %) [40,41]. These examples further suggests that disparities in strain to failure between the alloys investigated in this study are indeed the result of microstructure or AM processing related defects versus atomistic properties, however the influence of composition on ductility may play a role and will be subject of future studies on chemical homogenized samples (e.g. vacuum arc-remelting).

Additionally, considering the similarity in grain sizes between the two alloys, it is likely that processing defects instead of microstructure play a major role in reducing the strain to failure of the Ti_{0.4}Zr_{0.4}Nb_{0.1}Ta_{0.1} samples. For example, Ti_{0.4}Zr_{0.4}Nb_{0.1}Ta_{0.1} samples possess an average areal density of un-melted Nb and Ta particles of 6.5 % compared to Ti_{0.486}V_{0.375}Ta_{0.028}Cr_{0.111} which possess an areal density of 2.3 % (V and Ta particles) (Fig. 5a and e). As un-melted powder particles act as stress concentrations, they can lead to debonding and premature fracture [7,30,42], it is likely that these results explain the unexpectedly weak tensile behaviors for Ti_{0.4}Zr_{0.4}Nb_{0.1}Ta_{0.1} (e.g., brittle like fracture surfaces in Fig. 5d) versus $Ti_{0.486}V_{0.375}Ta_{0.028}Cr_{0.111}$ (e.g., quasi-cleavage fracture appearance, with localized plasticity in Fig. 5h). More analysis is necessary to understand the transfer of un-melted powders into the melt pool specifically for L-PBF AM (e.g., follow-on in-situ DXR experiments with elemental powder blends [43]), and to quantify their role in damage localization for multicomponent alloys leveraging refractory elemental powders. For example, it is well known that greater than a few percent porosity strongly influences tensile behaviors in AM materials [44]; however, corresponding data on the influence of un-melted powder defects is scarce in the literature. This is a significant, and largely understudied defect source that must be further explored given the prevalence of employing cost-effective elemental versus pre-alloyed powders in AM-RCCAs. Additional considerations on annealing and homogenization heat treatments to improve tensile ductility have shown promise for other AM-RCCAs [45] and may also be broadly applicable for the alloys investigated in this study.

4.2. Influence of chemical heterogeneity on local D-parameter

The above section highlights the challenge in fully eliminating defects in AM-RCCAs using elemental powder blends of high-melting temperature elements. Non-negligible amounts of un-melted powder particles present in the samples may lead to significant chemical heterogeneity which can locally influence plastic deformation mechanisms. For example, these local composition changes would result in a change in the D parameter, thus influencing the tendency for plastic deformation (e.g., ductile behavior versus brittle fracture) within the sample [39]. Furthermore, such local changes in compositions near un-melted powders could lead to significant risk of premature failure as they are near areas of significant stress concentration.

To better understand the role of chemical heterogeneity on the Dparameter, three representative EDS maps were conducted within representative samples of both alloys. These maps were selected from different regions in the build and avoided un-melted powder particles. As such, they can be considered the "bulk" composition, in the absence of un-melted powder particle defects. The regions selected for EDS are plotted in Fig. 7, while Table 4 shows the tabulated values of composition (in at. %) and the estimated D-parameter for each location. Overall, the compositions for both Ti_{0.4}Zr_{0.4}Nb_{0.1}Ta_{0.1} and Ti_{0.486}V_{0.375}. Ta_{0.028}Cr_{0.111} show significant fluctuation, particularly the high melting temperature elements. For example, Ta shows the largest deviation in at. % between each of the selected areas in Ti_{0.4}Zr_{0.4}Nb_{0.1}Ta_{0.1} (1.29-8.45 % versus the expected value of 10 %) and $Ti_{0.486}V_{0.375}Ta_{0.028}Cr_{0.111}$ (0.63-2.41 % versus the expected value of 2.8 %). Such behavior confirms the absence of melting for Ta powders locally, as this would also reduce the amount of Ta present within the melt. Similar trends also occur for the Nb powders in Ti_{0.4}Zr_{0.4}Nb_{0.1}Ta_{0.1}. Interestingly, this fluctuation of local refractory elements does not significantly modify the D-parameter. This is shown in Table 4, where the D-parameter is plotted for both alloy as a function of selected EDS mapping area. The Dparameter for $Ti_{0.4}Zr_{0.4}Nb_{0.1}Ta_{0.1}$ ranges from D=3.81-3.90 (between Area 1 to Area 3). In comparison, the D-parameter of Ti_{0.486}V_{0.375}- $Ta_{0.028}Cr_{0.111}$ ranges from D = 3.08-3.01 (between Area 1 to Area 3); importantly, these areas all possess values for D > 3.0. Overall, this data suggests that the bulk matrix of the alloys investigated in this study show ductility tendency consistent with the D-parameter prediction, but the

Table 4
Bulk EDS composition (at. %) and D-parameter for selected areas.

${\rm Ti_{0.4}Zr_{0.4}Nb_{0.1}Ta_{0.1}}$							
Area	Ti	Zr	Nb	Ta	D-parameter		
1	41.99	40.40	11.94	5.67	3.81		
2	44.78	37.72	9.05	8.45	3.82		
3	49.03	37.29	12.38	1.29	3.90		
$Ti_{0.486}V_{0.375}Ta_{0.028}Cr_{0.111}$							
Area	Ti	V	Cr	Ta	D-parameter		
					·		
1	49.92	36.03	14.42	0.63	3.08		
2	51.27	31.06	14.25	2.41	3.05		
3	50.45	36.12	11.61	1.82	3.01		

ductile performance is reduced by a combination of incomplete powder particle defects and composition variation. Such results show promise for future studies leveraging methods to maximize melting such as prealloyed powders or via optimized process variables/settings.

4.3. Comparison with other studies and extensions to Mo and W-containing RCCAs

The comparison between the alloys investigated in this study and tensile data for other RCCAs in the literature [11,30,46-48] is presented in Fig. 8. Although combination of strength and ductility in ${\rm Ti}_{0.486}{\rm V}_{0.375}{\rm Ta}_{0.028}{\rm Cr}_{0.111}$ outperforms other AM-RCCAs in the literature (Fig. 8), Ti_{0.4}Zr_{0.4}Nb_{0.1}Ta_{0.1} shows anomalous behaviors compared to other Ti–Zr–Nb–Ta alloys, in particular reduced strain to failure values. Note, the sample dimensions employed in this work are generally consistent with reported data from literature shown in Fig. 8. Data on tensile tests of AM alloys in Fig. 8 is from samples with dimensions comparable to our samples, although for conventionally processed alloys some investigators used relatively larger samples. Furthermore, recent work in the literature on L-PBF AM Ti-6Al-4V [49] shows that reducing the sample gage length does not increase tensile ductility but may actually reduce the measured tensile ductility. Therefore, the reported tensile ductility of the alloys investigated in this study represents a lower bound and the differences in the reported strength/ductility between alloys shown in Fig. 8 are not due to slightly different gage

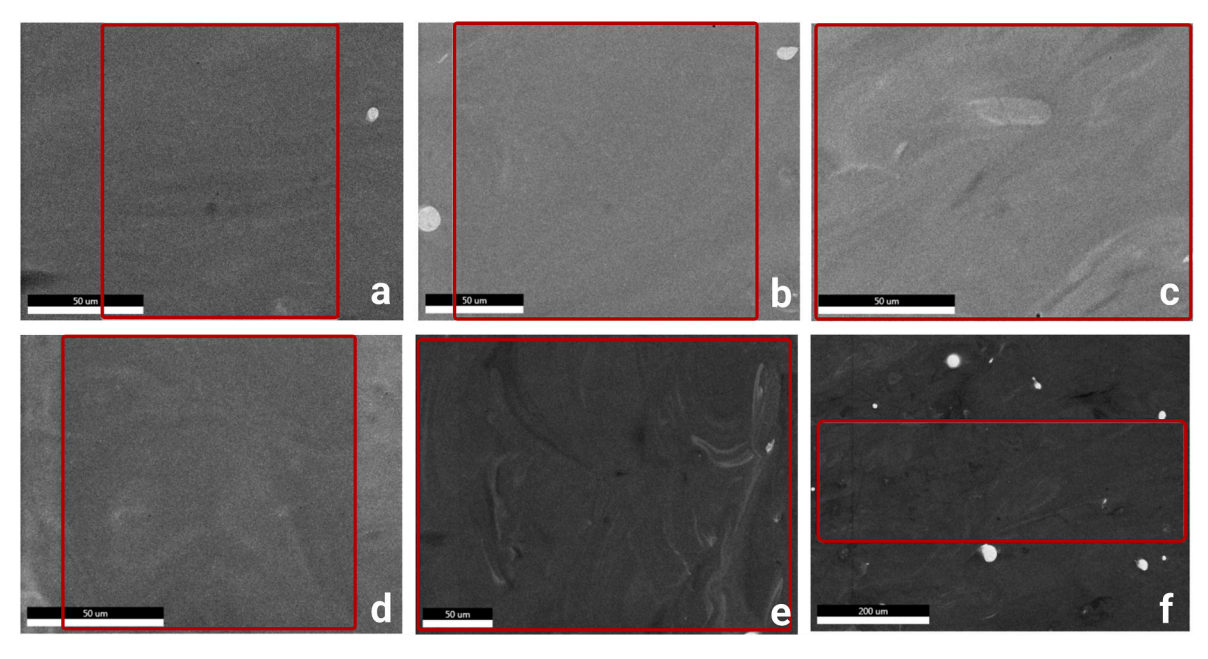


Fig. 7. Bulk composition EDS mapping of Areas 1, 2, and 3 for each alloy, namely: Ti_{0.4}Zr_{0.4}Nb_{0.1}Ta_{0.1} (a, b, and c) and Ti_{0.486}V_{0.375}Ta_{0.028}Cr_{0.111} (d, e, and f). Note: bold red outline signifies area selected for each EDS scan. (For interpretation of the references to color in this figure legend, the reader is referred to the Web version of this article.)

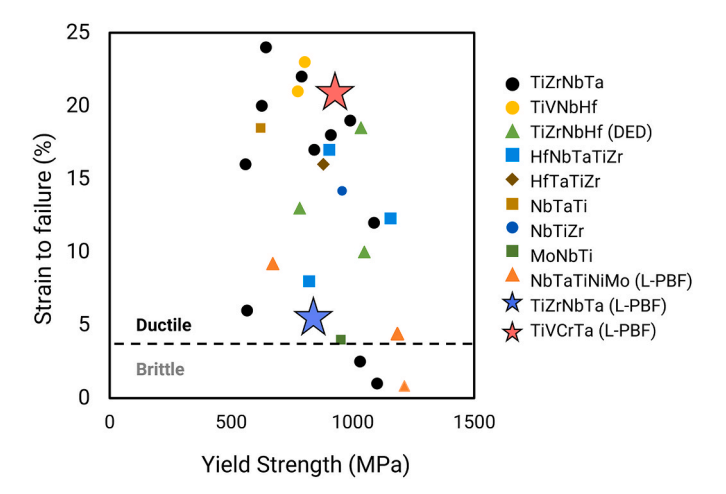


Fig. 8. Tensile yield strength versus strain to failure of $Ti_{0.4}Zr_{0.4}Nb_{0.1}Ta_{0.1}$ and $Ti0_{.486}V_{0.375}Ta_{0.028}Cr_{0.111}$ made by L-PBF AM compared to other Ti–Zr–Nb-Hf-Ta-Mo alloys in the literature manufactured through casting, DED, and L-PBF AM (refs: [10,11,30,32,47,48]). Brittle alloys described as those with <4 % strain to failure.

length and gage width dimensions used by different investigators.

As discussed above, it is likely that the large amounts of un-melted refractory elements contributing to the reduced failure strain values (and possibly overall tensile behavior). By analyzing additional compositions, it will become clearer which atomistic properties most strongly govern strength-ductility synergy and what advances in AM processing science are needed to enable fully dense AM-RCCAs. While important, such experiments are out of the scope of the current work but will be a major focus of future studies. Additionally, extensions to the rapid ductility screening framework are needed to develop RCCAs with large concentration of Mo and W, as these alloys are the most promising for high temperature applications [3,8,16,47,50].

Although alloys investigated in this study have melting temperatures well below that of Mo and W containing RCCAs, low melting temperature RCCAs can possess elevated temperature strength commensurate or surpassing current Ni-based superalloys such as IN718 and Haynes 230, which exhibit yield strengths of 1000 and 255 MPa up to 600 °C, respectively but both rapidly decrease below 200 MPa at temperatures above 800 °C and ultimately fail above 1200 °C [1]. At elevated temperatures, NbTa_{0.3}TiZr retains a yield strength of $\sigma_v = 274$ MPa at 1000 °C and $\sigma_v = 102$ MPa at 1200 °C although its melting temperature is 1711 °C. As such, even though our alloys' melting points are slightly below pure Ti, they are still 100–200 $^{\circ}\text{C}$ higher than that of Ni and Fe and their related alloys. Commercially used Ti-alloys, like Ti-64 and Ti-5553, at room temperature, have been shown to exhibit yield strengths around 900 MPa [51]. Overall, Ti-based RCCAs, such as those investigated in this study, show strong promise to replace conventional Ni- and Fe-based alloys under elevated temperatures. Additionally, certain untested compositions from our alloy screening approach for ductility and AM processibility (~100 alloys total) possess estimated melting temperatures as high as 1800 $^{\circ}\text{C}$ (Ti_{0.05}Zr_{0.65}Nb_{0.05}Ta_{0.25} which has D = 3.33 and freezing range of 39.4 °C), which were (obviously) not tested due to the high concentrations of elemental Ta. With further optimized process settings and additional material/machine considerations (such as the use of pre-alloyed powders or re-melting/preheating the build with the DiAM's secondary diode laser), such compositions can be addressed in the future while avoiding un-melted particle defects. Importantly, the two compositions selected in this study were chosen to be representative, thus additional alloys with improved properties (melting temperature, yield strength, ductility, etc.) are likely.

Nevertheless, Mo and W-containing RCCAs generally show enhanced strength retention at extreme temperatures required for next-generation energy and transportation applications such as the well know MoNbTaW

and MoNbTaVW that retain yield strengths >400 MPa at 1600 °C [3, 52-54]. However, most Mo and W containing alloys identified in our framework possess D < 3.0 and are therefore predicted to be brittle. However, recent work on L-PBF of NbTaTiNiMo₁₀ displayed maximum failure strain under tensile loading of 4.4 % [47]. As only the {110} slip system is considered in this work, extensions to our atomistic screening framework including additional BCC slip systems have great potential to take advantage of newly discovered dislocation pathways within RCCAs such as the equiatomic Ti-Nb-Mo system, which possesses D parameter ~2.9 but has shown tensile ductility under nanomechanical tensile testing in Ref. [55]. Such analyses on additional compositions will also increase our understanding of potential limitations of our D > 3.0ductility hypothesis. Such extensions will need to be paired with additional considerations for manufacturability outlined in this work to reduce hot-cracking, porosity, and un-melted powder defects (e.g., via pre-alloyed powders, further optimizing processing variables, or select post-processing treatments). As such, the reduction of both laser-matter interaction and starting material defects will be necessary to enable AM-RCCAs employing high-melting point Mo and W refractory elements.

5. Conclusions

Overall, this work provides a physics-based, predictive framework for additive manufacturing of non-equiatomic RCCAs with room temperature ductility compared to prior trial-and-error approaches. Two representative alloys were down selected for tensile ductility and AM processability from $\sim\!10^6$ potential compositions from the Ti–Zr–Nb–Ta–V–Cr system using an alloy design strategy encompassing multiple optimization objectives. Overall, the following conclusions can be made.

- Atomistic modeling based on a *D*-parameter greater than 3.0 showed good agreement with tensile ductility in two representative non-equiatomic RCCAs (Ti_{0.4}Zr_{0.4}Nb_{0.1}Ta_{0.1} and Ti_{0.486}V_{0.375}Ta_{0.028}Cr_{0.111}) made by L-PBF AM.
- As-built samples from both alloys possessed yield strengths >800 MPa and strains to failure >5 %, values which match or exceed other AM-RCCAs in the literature. Ti_{0.486}V_{0.375}Ta_{0.028}Cr_{0.111} possessed higher yield strength than Ti_{0.4}Zr_{0.4}Nb_{0.1}Ta_{0.1} due to an increased unstable stacking fault energy.
- Laser-material interaction defects (i.e., LOF and keyhole porosity) for both alloys follow systematic trends in P–V processing space. *In situ* DXR imaging and analytical melt pool simulation for lack of fusion and keyhole melt pool boundary showed good agreement.
- The differences in the measured tensile strain to failure between the
 two alloys, are attributed, in part, to the presence of a small volume
 fraction of incomplete powder particle melting and chemical inhomogeneity within the build. This highlights the need to mitigate
 manufacturing defects in the 3D printed alloys when using elemental
 powder mixtures of high-melting point metals.

These results highlight the success of our alloy design framework to guide the selection of AM-RCCAs with room temperature ductility potency that can be manufactured without solidification induced cracking under rapid solidification processing. Although this work focused on non-equiatomic RCCAs with low melting temperatures (<2000 °C), our framework can be extended to high-melting temperature alloys (e.g., containing large portions of Mo and W elements) by considering additional BCC slip systems. Therefore, validation of this framework in the context of Mo and W-containing alloys is expected to enable transformative impacts of AM-RCCAs with both room temperature ductility and enhanced high-temperature performance.

CRediT authorship contribution statement

Dillon Jobes: Writing - review & editing, Validation, Software, Investigation, Formal analysis, Data curation. Daniel Rubio-Ejchel: Writing - review & editing, Investigation, Formal analysis, Data curation. Lucero Lopez: Investigation. William Jenkins: Investigation, Formal analysis, Data curation, Aditya Sundar: Software, Investigation, Formal analysis, Data curation. Christopher Tandoc: Software, Investigation, Formal analysis, Data curation. Jacob Hochhalter: Supervision, Project administration, Investigation. Amit Misra: Writing original draft, Supervision, Project administration, Funding acquisition. Liang Qi: Writing – review & editing, Software, Project administration, Funding acquisition. Yong-Jie Hu: Writing - review & editing, Supervision, Software, Project administration, Investigation, Formal analysis, Data curation, Conceptualization. Jerard V. Gordon: Writing – review & editing, Writing – original draft, Visualization, Supervision, Software, Project administration, Methodology, Investigation, Funding acquisition, Formal analysis, Data curation, Conceptualization.

Declaration of competing interest

The authors have no known competing financial interests or personal relationships that could have appeared to influence the work reported in this paper.

Data availability

Data will be made available on request.

Acknowledgements

The authors would like to thank John Roehling, Joe McKeown, and Thomas Voisin from Lawrence Livermore National Laboratory for assistance with AM processing on the DiAM system and helpful comments. The authors would also like to thank Samuel J. Clark and Kamel Fezza beamline scientists at APS 32-ID and Joseph Aroh from The Naval Research Laboratory for help with DXR data analysis. This work was partially supported by NSF DMR-2316762 as well as the startup fund from Drexel University. This research used resources of the Advanced Photon Source; a U.S. Department of Energy (DOE) Office of Science User Facility operated for the DOE Office of Science by Argonne National Laboratory under Contract No. DE-AC02-06CH11357.

References

- [1] O.N. Senkov, G.B. Wilks, J.M. Scott, D.B. Miracle, Mechanical properties of Nb25Mo25Ta25W25 and V20Nb20Mo20Ta20W20 refractory high entropy alloys, Intermetallics 19 (2011) 698-706, https://doi.org/10.1016/J. INTERMET.2011.01.004.
- [2] D.H. Cook, P. Kumar, M.I. Payne, C.H. Belcher, P. Borges, W. Wang, F. Walsh, Z. Li, A. Devaraj, M. Zhang, M. Asta, A.M. Minor, E.J. Lavernia, D. Apelian, R.O. Ritchie, Kink bands promote exceptional fracture resistance in a NbTaTiHf refractory medium-entropy alloy, Science 384 (2024) 178-184, https://doi.org/10.1126/ 28/SUPPL_FILE/SCIENCE.ADN2428_SM.PDF.
- [3] O.N. Senkov, G.B. Wilks, D.B. Miracle, C.P. Chuang, P.K. Liaw, Refractory highentropy alloys, Intermetallics 18 (2010) 1758-1765, https://doi.org/10.1016/J. INTERMET.2010.05.014.
- Y. Chen, Y.T. Tang, D.M. Collins, S.J. Clark, W. Ludwig, R. Rodriguez-Lamas, C. Detlefs, R.C. Reed, P.D. Lee, P.J. Withers, C. Yildirim, High-resolution 3D strain and orientation mapping within a grain of a directed energy deposition laser additively manufactured superalloy, Scr Mater 234 (2023), https://doi.org/ 10.1016/i.scriptamat.2023.115579.
- [5] E.P. George, D. Raabe, R.O. Ritchie, High-entropy alloys, Nat. Rev. Mater. 4 (2019)
- 515–534, https://doi.org/10.1038/s41578-019-0121-4.
 [6] J.P. Couzinié, G. Dirras, L. Perrière, T. Chauveau, E. Leroy, Y. Champion, I. Guillot, Microstructure of a near-equimolar refractory high-entropy alloy, Mater. Lett. 126 (2014) 285-287, https://doi.org/10.1016/j.matlet.2014.04.062
- M.A. Melia, S.R. Whetten, R. Puckett, M. Jones, M.J. Heiden, N. Argibay, A. B. Kustas, High-throughput additive manufacturing and characterization of refractory high entropy alloys, Appl. Mater. Today 19 (2020) 100560, https://doi. org/10.1016/j.apmt.2020.100560.

- [8] H. Zhang, W. Xu, Y. Xu, Z. Lu, D. Li, The thermal-mechanical behavior of WTaMoNb high-entropy alloy via selective laser melting (SLM): experiment and simulation, Int. J. Adv. Manuf. Technol. 96 (2018) 461-474, https:// 0.1007/S00170-017-1331-9/METRICS
- [9] O.N. Senkov, D.B. Miracle, K.J. Chaput, J.P. Couzinie, Development and exploration of refractory high entropy alloys - a review, J. Mater. Res. 33 (2018) 3092-3128, https://doi.org/10.1557/imr.2018.15
- [10] S. Gou, M. Gao, Y. Shi, S. Li, Y. Fang, X. Chen, H. Chen, W. Yin, J. Liu, Z. Lei, H. Wang, Additive manufacturing of ductile refractory high-entropy alloys via phase engineering, Acta Mater. 248 (2023), https://doi.org/10.1016/j.
- [11] O.N. Senkov, D.B. Miracle, S.I. Rao, Correlations to improve room temperature ductility of refractory complex concentrated alloys, Materials Science and Engineering: A 820 (2021), https://doi.org/10.1016/j.msea.2021.141512.
- J. Pyeon, Joseph Aroh, R. Jiang, A.K. Verma, B. Gould, A. Ramlatchan, Kamel Fezzaa, N. Parab, C. Zhao, T. Sun, A.D. Rollett, K. Fezzaa, Time-resolved geometric feature tracking elucidates laser-induced keyhole dynamics, Integr Mater Manuf Innov 10 (2021) 677-688, https://doi.org/10.1007/s40192-021-
- [13] Y.J. Hu, A. Sundar, S. Ogata, L. Qi, Screening of generalized stacking fault energies, surface energies and intrinsic ductile potency of refractory multicomponent alloys, Acta Mater. 210 (2021), https://doi.org/10.1016/j.actamat.2021.116800.
- [14] A. Sundar, D.B. Ferron, Y.J. Hu, L. Qi, Automated hierarchical screening of refractory multicomponent alloys with high intrinsic ductility and surface passivation potency, MRS Commun 12 (2022) 1086-1095, https://doi.org/ 10 1557/s43579-022-00241-1.
- C. Tandoc, Y.J. Hu, L. Qi, P.K. Liaw, Mining of lattice distortion, strength, and intrinsic ductility of refractory high entropy alloys, npj Comput. Mater. 9 (1 9) (2023) 1–12, https://doi.org/10.1038/s41524-023-00993-x, 2023.
- [16] C. Yang, L. Qi, Ab initio calculations of ideal strength and lattice instability in W-Ta and W-Re alloys, Phys. Rev. B 97 (2018) 014107, https://doi.org/10.1103 PHYSREVB.97.014107/FIGURES/15/MEDIUM.
- [17] L. Qi, D.C. Chrzan, Tuning ideal tensile strengths and intrinsic ductility of bcc refractory alloys, Phys. Rev. Lett. 112 (2014) 115503, https://doi.org/10.1103/ PHYSREVLETT.112.115503/FIGURES/3/MEDIUM.
- [18] O.N. Senkov, D.B. Miracle, Generalization of intrinsic ductile-to-brittle criteria by Pugh and Pettifor for materials with a cubic crystal structure, Sci. Rep. 11 (2021) 10-13, https://doi.org/10.1038/s41598-021-83953-z.
- Y.J. Hu, A. Sundar, S. Ogata, L. Qi, Screening of generalized stacking fault energies, surface energies and intrinsic ductile potency of refractory multicomponent alloys, Acta Mater, 210 (2021) 116800, https://doi.org/10.1016/j.actamat.2021.116800.
- [20] J.-O. Andersson, T. Helander, L. Höglund, P. Shi, B. Sundman, Thermo-Calc & DICTRA, computational tools for materials science, Calphad 26 (2002).
- [21] B. Dovgyy, M. Simonelli, M.S. Pham, Alloy design against the solidification cracking in fusion additive manufacturing: an application to a FeCrAl alloy, Mater Res Lett 9 (2021) 350–357, https://doi.org/10.1080/21663831.2021.1922945
- S. Kou, A criterion for cracking during solidification, Acta Mater. 88 (2015) 366-374, https://doi.org/10.1016/J.ACTAMAT.2015.01.034
- G. Tang, B.J. Gould, A. Ngowe, A.D. Rollett, An updated index including toughness for hot-cracking susceptibility, Metall Mater Trans A Phys Metall Mater Sci 53 (2022) 1486-1498, https://doi.org/10.1007/s11661-022-06612-6.
- [24] N. Kouraytem, P.J. Chiang, R. Jiang, C. Kantzos, J. Pauza, R. Cunningham, Z. Wu, G. Tang, N. Parab, C. Zhao, K. Fezzaa, T. Sun, A.D. Rollett, Solidification crack propagation and morphology dependence on processing parameters in AA6061 from ultra-high-speed x-ray visualization, Addit. Manuf. 42 (2021), https://doi. rg/10.1016/j.addma.2021.101959.
- [25] C. Zhao, K. Fezzaa, R.W. Cunningham, H. Wen, F. De Carlo, L. Chen, A.D. Rollett, T. Sun, Real-time monitoring of laser powder bed fusion process using high-speed X-ray imaging and diffraction, Sci. Rep. 7 (2017), https://doi.org/10.1038/
- [26] R. Cunningham, C. Zhao, N. Parab, C. Kantzos, J. Pauza, K. Fezzaa, T. Sun, A. D. Rollett, Keyhole threshold and morphology in laser melting revealed by ultrahigh-speed x-ray imaging. https://www.science.org, 2019.
- J.V. Gordon, S.P. Narra, R.W. Cunningham, H. Liu, H. Chen, R.M. Suter, J.L. Beuth, A.D. Rollett, Defect structure process maps for laser powder bed fusion additive manufacturing, Addit. Manuf. 36 (2020) 101552, https://doi.org/10.1016/j. addma.2020.101552.
- [28] B.J. Simonds, J. Tanner, A. Artusio-Glimpse, P.A. Williams, N. Parab, C. Zhao, T. Sun, The causal relationship between melt pool geometry and energy absorption measured in real time during laser-based manufacturing, Appl. Mater. Today 23 (2021), https://doi.org/10.1016/j.apmt.2021.101049.
- [29] H. Dobbelstein, E.L. Gurevich, E.P. George, A. Ostendorf, G. Laplanche, Laser metal deposition of compositionally graded TiZrNbTa refractory high-entropy alloys using elemental powder blends, Addit. Manuf. 25 (2019) 252-262, https://doi. rg/10.1016/j.addma.2018.10.042
- [30] F. Wang, T. Yuan, R. Li, S. Lin, P. Niu, V. Cristino, Effect of Mo on the morphology, microstructure and mechanical properties of NbTa0.5TiMox refractory high entropy alloy fabricated by laser powder bed fusion using elemental mixed powders, Int. J. Refract. Metals Hard Mater. 111 (2023), https://doi.org/10.1016/ irmhm, 2023, 106107.
- [31] M.J. Matthews, G. Guss, D.R. Drachenberg, J.A. Demuth, J.E. Heebner, E.B. Duoss, J.D. Kuntz, C.M. Spadaccini, Diode-based additive manufacturing of metals using an optically-addressable light valve, Opt Express 25 (2017) 11788, https://doi. oe.25.011
- [32] Z. Li, W. Lai, X. Tong, D. You, W. Li, X. Wang, Design of TiZrNbTa multi-principal element alloys with outstanding mechanical properties and wear resistance,

- Materials Science and Engineering: A 845 (2022), https://doi.org/10.1016/j.
- [33] O.N. Senkov, J.M. Scott, S.V. Senkova, D.B. Miracle, C.F. Woodward, Microstructure and room temperature properties of a high-entropy TaNbHfZrTi alloy, J. Alloys Compd. 509 (2011) 6043–6048, https://doi.org/10.1016/j. jallcom.2011.02.171.
- [34] V.T. Nguyen, M. Qian, Z. Shi, X.Q. Tran, D.M. Fabijanic, J. Joseph, D.D. Qu, S. Matsumura, C. Zhang, F. Zhang, J. Zou, Cuboid-like nanostructure strengthened equiatomic Ti–Zr–Nb–Ta medium entropy alloy, Materials Science and Engineering: A 798 (2020), https://doi.org/10.1016/j.msea.2020.140169.
- [35] X. Luo, C. Yang, R.Y. Li, H. Wang, H.Z. Lu, T. Song, H.W. Ma, D.D. Li, A. Gebert, Y. Y. Li, Effect of silicon content on the microstructure evolution, mechanical properties, and biocompatibility of β-type TiNbZrTa alloys fabricated by laser powder bed fusion, Biomater. Adv. 133 (2022) 112625, https://doi.org/10.1016/ J.MSFC.2021.112625.
- [36] J. González-Masís, J.M. Cubero-Sesin, A. Campos-Quirós, K. Edalati, Synthesis of biocompatible high-entropy alloy TiNbZrTaHf by high-pressure torsion, Materials Science and Engineering: A 825 (2021), https://doi.org/10.1016/j. msea 2021 141869
- [37] A. Kareer, J.C. Waite, B. Li, A. Couet, D.E.J. Armstrong, A.J. Wilkinson, Short communication: 'Low activation, refractory, high entropy alloys for nuclear applications, J. Nucl. Mater. 526 (2019) 151744, https://doi.org/10.1016/J. JNUCMAT.2019.151744.
- [38] J. Ru, R. Ma, M. Wan, Q. Xie, First principles calculation on electronic structures and mechanical properties of TiCrTaV high–entropy alloy, Mater. Today Commun. 31 (2022) 103801, https://doi.org/10.1016/J.MTCOMM.2022.103801.
- [39] Y.J. Hu, A. Sundar, S. Ogata, L. Qi, Screening of generalized stacking fault energies, surface energies and intrinsic ductile potency of refractory multicomponent alloys, Acta Mater. 210 (2021) 1–45, https://doi.org/10.1016/j.actamat.2021.116800.
- [40] Y.D. Wu, Y.H. Cai, T. Wang, J.J. Si, J. Zhu, Y.D. Wang, X.D. Hui, A refractory Hf25Nb25Ti25Zr25 high-entropy alloy with excellent structural stability and tensile properties, Mater. Lett. 130 (2014) 277–280, https://doi.org/10.1016/j. matlet 2014 05 134
- [41] S. Sheikh, S. Shafeie, Q. Hu, J. Ahlström, C. Persson, J. Veselý, J. Zýka, U. Klement, S. Guo, Alloy design for intrinsically ductile refractory high-entropy alloys, J. Appl. Phys. 120 (2016), https://doi.org/10.1063/1.4966659.
- [42] P. Rebesan, M. Ballan, M. Bonesso, A. Campagnolo, S. Corradetti, R. Dima, C. Gennari, G.A. Longo, S. Mancin, M. Manzolaro, G. Meneghetti, A. Pepato, E. Visconti, M. Vedani, Pure molybdenum manufactured by Laser Powder Bed Fusion: thermal and mechanical characterization at room and high temperature, Addit. Manuf. 47 (2021). https://doi.org/10.1016/j.addma.2021.102277.
- [43] H. Wang, B. Gould, M. Moorehead, M. Haddad, A. Couet, S.J. Wolff, In situ X-ray and thermal imaging of refractory high entropy alloying during laser directed deposition, J. Mater. Process. Technol. 299 (2022), https://doi.org/10.1016/j. imatprotec.2021.117363.

- [44] A.Y. Al-Maharma, S.P. Patil, B. Markert, Effects of porosity on the mechanical properties of additively manufactured components: a critical review, Mater. Res. Express 7 (2020), https://doi.org/10.1088/2053-1591/abcc5d.
- [45] Y. Zhang, H. Wang, Y. Zhu, S. Zhang, F. Cheng, J. Yang, B. Su, C. Yang, High specific yield strength and superior ductility of a lightweight refractory highentropy alloy prepared by laser additive manufacturing, Addit. Manuf. 77 (2023), https://doi.org/10.1016/j.addma.2023.103813.
- [46] H. Zhang, Y. Zhao, J. Cai, S. Ji, J. Geng, X. Sun, D. Li, High-strength NbMoTaX refractory high-entropy alloy with low stacking fault energy eutectic phase via laser additive manufacturing, Mater. Des. 201 (2021) 109462, https://doi.org/ 10.1016/j.matdes.2021.109462.
- [47] H. Zhang, J. Cai, J. Geng, X. Sun, Y. Zhao, X. Guo, D. Li, Development of high strength high plasticity refractory high entropy alloy based on Mo element optimization and advanced forming process, Int. J. Refract. Metals Hard Mater. 112 (2023) 106163, https://doi.org/10.1016/J.IJRMHM.2023.106163.
- [48] S. Gou, M. Gao, Y. Shi, S. Li, Y. Fang, X. Chen, H. Chen, W. Yin, J. Liu, Z. Lei, H. Wang, Additive manufacturing of ductile refractory high-entropy alloys via phase engineering, Acta Mater. 248 (2023), https://doi.org/10.1016/j. actamat.2023.118781.
- [49] D. Barba, C. Alabort, Y.T. Tang, M.J. Viscasillas, R.C. Reed, E. Alabort, On the size and orientation effect in additive manufactured Ti-6Al-4V, Mater. Des. 186 (2020), https://doi.org/10.1016/j.matdes.2019.108235.
- [50] M. Moorehead, K. Bertsch, M. Niezgoda, C. Parkin, M. Elbakhshwan, K. Sridharan, C. Zhang, D. Thoma, A. Couet, High-throughput synthesis of Mo-Nb-Ta-W high-entropy alloys via additive manufacturing, Mater. Des. 187 (2020) 108358, https://doi.org/10.1016/J.MATDES.2019.108358.
- [51] A.-F. Gerday, Mechanical behavior of Ti-5553 alloy Modeling of representative cells. http://www.argenco.ulg.ac.be, 2009.
- [52] Q. Liu, G. Wang, X. Sui, Y. Liu, X. Li, J. Yang, Microstructure and mechanical properties of ultra-fine grained MoNbTaTiV refractory high-entropy alloy fabricated by spark plasma sintering, J. Mater. Sci. Technol. 35 (2019) 2600–2607, https://doi.org/10.1016/j.jmst.2019.07.013.
- [53] J. Han, B. Su, J. Lu, J. Meng, A. Zhang, Y. Wu, Preparation of MoNbTaW refractory high entropy alloy powders by pressureless spark plasma sintering: crystal structure and phase evolution, Intermetallics 123 (2020), https://doi.org/ 10.1016/j.intermet.2020.106832.
- [54] O.N. Senkov, G.B. Wilks, J.M. Scott, D.B. Miracle, Mechanical properties of Nb2SMo25Ta 25W25 and V20Nb20Mo 20Ta20W20 refractory high entropy alloys, Intermetallics 19 (2011) 698–706, https://doi.org/10.1016/j. intermet.2011.01.004.
- [55] F. Wang, G.H. Balbus, S. Xu, Y. Su, J. Shin, P.F. Rottmann, K.E. Knipling, J. C. Stinville, L.H. Mills, O.N. Senkov, I.J. Beyerlein, T.M. Pollock, D.S. Gianola, Multiplicity of dislocation pathways in a refractory multiprincipal element alloy, Science 370 (1979) 95–101, https://doi.org/10.1126/science.aba3722, 2020.